

A SEMI-DISCRETE OPTIMAL TRANSPORT SCHEME FOR THE SEMI-GEOSTROPHIC SLICE COMPRESSIBLE MODEL

THÉO LAVIER* AND BEATRICE PELLONI†

ABSTRACT. We develop a semi-discrete optimal transport scheme for the compressible semi-geostrophic equations, a system that plays an important role in modelling large-scale atmospheric dynamics and frontogenesis. Unlike the incompressible case, the compressible equations involve variable density and internal energy, but can be recast into a variational framework that naturally couples the dynamics with an optimal transport formulation. This is done by a change to the so-called geostrophic coordinates, via a transformation inspired by the incompressible case. The discrete version of this variational formulation provides the basis for a numerical particle scheme. The implementation of this scheme presents considerable challenges, due to a non-quadratic cost function and parabolic c -Laguerre cells. To address these challenges, we use c -exponential charts to construct c -Laguerre tessellations efficiently, ensuring conservation of mass and energy while preserving key geometric structures. We analyse the scheme and validate its convergence through numerical experiments, including a single-seed benchmark and error analysis. This work provides a significant new generalisation of existing semi-discrete optimal transport techniques, offering a robust and structure-preserving tool for simulating realistic atmospheric flows.

1. INTRODUCTION

1.1. Background and motivation. The compressible semi-geostrophic (SG) equations constitute a fundamental framework for modelling large-scale atmospheric dynamics, particularly in applications involving frontogenesis and the evolution of geophysical flows past the time of weather front formation. In contrast with their incompressible counterparts, the compressible SG equations include variable density and internal energy, capturing essential thermodynamic processes. This added complexity is crucial for realistic atmospheric simulations but poses significant challenges in both the theoretical analysis and the numerical modelling of the equations.

Over the past decades, optimal transport techniques have emerged as powerful tools for constructing structure-preserving numerical schemes in fluid dynamics [1, 10]. Earlier work by [9, 15] demonstrated the efficacy of semi-discrete optimal transport methods in the context of the incompressible SG equations, using Laguerre tessellations to generate transport maps that conserve mass and energy. The theoretical foundations and convergence results from [12, 17], have consolidated the viability of numerical semi-discrete optimal transport methods. There has also been significant progress made on using full discrete optimal transport methods to simulate semi-geostrophic systems [2, 3, 6]. The fully compressible SG system was first studied in [8], a work that clarified both the mathematical intricacies and the meteorological importance of this system. Recent contributions by [7, 18] provided test cases for frontogenesis in vertical slices, stressing the need to account for compressibility in realistic atmospheric models.

A numerical particle scheme based on semi-discrete optimal transport techniques, first implemented for the incompressible SG system [9, 15], was recently extended to the compressible system in [5], laying the foundation for the developments presented here. Specifically, the present paper builds on the results presented in [5] by developing a novel semi-discrete optimal transport scheme specifically tailored for the compressible SG equations. This is done by transforming the governing equations to geostrophic coordinates, an approach inspired by the seminal work of Hoskins [11], whereby the complex interplay between density, temperature, and velocity is

(*) LABORATOIRE IMATH, UNIVERSITÉ DE TOULON, TOULON, FRANCE

(†) MAXWELL INSTITUTE FOR MATHEMATICAL SCIENCES AND DEPARTMENT OF MATHEMATICS, HERIOT-WATT UNIVERSITY, EDINBURGH, UK

captured within a variational framework. A central challenge in this formulation is that the optimal transport problem associated with the compressible dynamics is defined by a cost function that incorporates gravitational potential and compressibility effects but is not reducible to the classical quadratic cost appearing in the incompressible case. This cost function implies that the resulting discrete version of the problem involves optimal tessellation with cells bounded by segments of parabolic curves. The associated theoretical and computational challenges are new and specific to the compressible case. To address these issues, our scheme incorporates internal energy as a dynamic variable, ensuring consistency with the first law of thermodynamics while preserving the underlying geometric and energetic structures of the system.

The contributions presented in this paper are in three parts. In the first part, we present what is, to our knowledge, the first semi-discrete optimal transport scheme for the 2D compressible SG equations in any setting, thereby advancing significantly the possibility to simulate realistic atmospheric flows. In the second part, we develop efficient computational techniques for constructing tessellations associated with non-quadratic cost functions, a key innovation that ensures numerical stability and accuracy. In the third part, we validate the convergence and the energy-conserving properties of the method through a series of numerical experiments, indicating the potential for application in large-scale atmospheric simulations.

1.2. Outline of the Paper. This paper is organized as follows. In Section 2, we introduce the SG compressible slice equations, a reduced 2D model for a compressible, stratified, and rotating atmosphere. These equations are derived directly from the compressible Euler equations by applying the hydrostatic, vertical slice, and semi-geostrophic approximations. We show how the coordinate transformation to geostrophic variables leads naturally to a variational formulation involving an optimal transport problem. In Section 3, we describe the semi-discrete optimal transport techniques and ideas underlying our numerical algorithm, detailing the construction of c -Laguerre tessellations and the introduction of c -exponential charts. Finally, in Section 4 we specify the initial conditions and parameter choices used in our simulations and we validate the approach through numerical experiments, including a single-seed benchmark and error analysis using the Wasserstein-2 metric, before discussing representative simulation results.

We also include an appendix containing several key lemmas. As a consequence of these lemmas, volume integrals are reduced to boundary integrals via the divergence theorem, thereby enabling efficient computation of the dual functional and its derivatives.

2. SLICE COMPRESSIBLE MODEL

In this section we derive a system of equations designed to model key compressible atmospheric dynamics within a two-dimensional vertical slice, while respecting hydrostatic balance and incorporating a semi-geostrophic approximation to isolate the large-scale balanced flow relevant to frontogenesis. It is notable that this model is not obtained through a reduction of the three-dimensional fully compressible SG system of [8], instead it is derived directly from the compressible Euler equations, following [7]. The introduction of a vertical slice geometry is necessary because a quasi-2D solution, as can be found in the incompressible case [9], cannot be derived by simple reduction of the 3D compressible model. More details on this derivation can be found in [14].

2.1. Governing Equations and Physical Assumptions. We begin with the three-dimensional *compressible Euler equations*, formulated for a stratified, rotating atmosphere. The state of the system at a point $\mathbf{x} = (x_1, x_2, x_3)$, corresponding to longitude, latitude, and altitude, respectively, is described by the velocity field $\mathbf{u} = (u, v, w)$, the density ρ , and the potential temperature θ . The thermodynamic state is closed by the equation of state for a dry ideal gas, which relates the pressure p to the density and temperature via the Exner pressure Π and is given by

$$p = \rho R_d \theta \Pi, \tag{2.1}$$

$$\Pi(\rho, \theta) = \left(\frac{\rho R_d \theta}{p_0} \right)^{\gamma-1},$$

where p_0 is a reference pressure, $\gamma = c_p/c_v$ is the adiabatic index, and $R_d = c_p - c_v$ is the specific gas constant for dry air.

We adopt from the start the hydrostatic approximation, which assumes a balance between the vertical pressure gradient and gravity. Under this assumption, the governing equations in a reference frame rotating with frequency f_{cor} about the vertical axis $\hat{\mathbf{e}}_3$ are the following:

$$\begin{cases} D_t \mathbf{u} + f_{\text{cor}} \hat{\mathbf{e}}_3 \times \mathbf{u} + c_p \theta \nabla \Pi + g \hat{\mathbf{e}}_3 = 0, \\ \partial_t \rho + \nabla \cdot (\rho \mathbf{u}) = 0, \\ D_t \Theta = 0, \end{cases} \quad (2.2)$$

where the material derivative D_t is given by :

$$D_t = \frac{\partial}{\partial t} + \mathbf{u} \cdot \nabla = \frac{\partial}{\partial t} + u \frac{\partial}{\partial x_1} + v \frac{\partial}{\partial x_2} + w \frac{\partial}{\partial x_3}. \quad (2.3)$$

2.1.1. Vertical Slice and Semi-Geostrophic Approximation. To derive the model analysed in this paper, we first apply the *vertical slice approximation*. As in [7], we consider a two-dimensional domain

$$\mathcal{X} := [-L, L] \times [0, H], \quad (2.4)$$

which represents a vertical slice of the atmosphere in the x_1 - x_3 plane. The model is periodic in the x_1 -direction and we assume rigid boundaries at the top and bottom. The velocity field $\mathbf{u} = (u, v, w)$ is decomposed into its in-slice component $\mathbf{u}_S = (u, w)$, and the transverse component, v .

The key assumption made to derive the model is that all fields are independent of the transverse coordinate x_2 , except for a background temperature gradient that is necessary to support baroclinic instability. Accordingly, the in-slice velocity \mathbf{u}_S , density ρ , and the in-slice potential temperature perturbation θ are assumed to depend only on (x_1, x_3, t) . The total potential temperature Θ is decomposed as

$$\Theta(x_1, x_2, x_3, t) = \theta_0 + \bar{\theta}(x_2) + \theta(x_1, x_3, t), \quad (2.5)$$

where θ_0 is a constant reference temperature and $\bar{\theta}(x_2) = sx_2$ is a background stratification profile, with s representing the background vertical shear. The model is then formulated in terms of the in-slice perturbation θ .

The momentum equations in the full model are replaced by the following balance relations:

$$v = \frac{1}{f_{\text{cor}}} c_p \theta \partial_{x_1} \Pi, \quad (2.6)$$

$$\theta = -\frac{g}{c_p \partial_{x_3} \Pi}. \quad (2.7)$$

The *semi-geostrophic slice compressible model*, introduced in [7, Remark 5.3], is derived from the Euler equations (Eq. (2.2)) by enforcing the assumptions above, using the SG approximation (Eq. (2.6) and Eq. (2.7)), and adding an *ad hoc* term to the right hand side of Eq. (2.2) motivated by analogy with the benchmark incompressible Eady Slice model of [9]. This additional term reduces the mean horizontal flow. The model is given by

$$\begin{cases} D_t v + f_{\text{cor}} u = s c_p (\Pi - \Pi_0) & \text{in } \mathcal{X} \times [0, t_f], \end{cases} \quad (2.8a)$$

$$\begin{cases} D_t \theta + s v = 0 & \text{in } \mathcal{X} \times [0, t_f], \end{cases} \quad (2.8b)$$

$$\begin{cases} D_t \rho + \rho \nabla \cdot \mathbf{u}_S = 0 & \text{in } \mathcal{X} \times [0, t_f], \end{cases} \quad (2.8c)$$

$$\begin{cases} c_p \theta \nabla \Pi = (f_{\text{cor}} v, -g)^T & \text{in } \mathcal{X} \times [0, t_f], \end{cases} \quad (2.8d)$$

$$\begin{cases} \mathbf{u}_S \cdot \hat{\mathbf{n}} = 0 & \text{on } \mathcal{X} \times [0, t_f] \cap \{x_3 = 0, H\}, \end{cases} \quad (2.8e)$$

$$\begin{cases} \mathbf{u}_S(-L, x_3) = \mathbf{u}_S(L, x_3) & \text{on } \mathcal{X} \times [0, t_f]. \end{cases} \quad (2.8f)$$

Here $D_t = \frac{\partial}{\partial t} + \mathbf{u}_S \cdot \nabla_2 = \partial_t + u\partial_{x_1} + w\partial_{x_3}$ is the in-slice material derivative and Π_0 is the initial spatial average of the Exner pressure, namely

$$\Pi_0 = \int_{\mathcal{X}} \Pi \, d\mathbf{x}, \quad (2.9)$$

which is included to reduce the mean horizontal flow. In this formulation, the transverse velocity v is influenced by both the Coriolis force and the background shear s .

In what follows, we assume the existence of a solution of this system and we focus on deriving and studying a particle scheme for its numerical approximation.

2.2. Formulation in geostrophic variables. For the analysis of SG, both incompressible and compressible, the key step is the formulation in a different set of variables. These variables were first introduced by Hoskins in [11], but the full potential of this formulation was only understood in groundbreaking work of Benamou and Brenier [1]. In these new, geostrophic variables, the incompressible 3D system is formulated as a continuity equation for the potential vorticity coupled with an optimal transport problem, with respect to a quadratic cost, between a fixed source measure and the time-dependent measure defined by the potential vorticity, denoted below by $\alpha(\mathbf{x}, t)$.

In general, the optimal transport involves pushing forward a source measure, denoted by $\sigma(\mathbf{x}, t)$, to the target measure $\alpha(\mathbf{x}, t)$ in a way that minimises the overall cost \mathcal{T}_c as defined by the associated cost function $c(\mathbf{x}, \mathbf{y})$, given by

$$\mathcal{T}_c = \min_{(T_t) \# \sigma_t = \alpha_t} \int_{\mathcal{X}} c(\mathbf{x}, T_t(\mathbf{x})) \, d\sigma_t(\mathbf{x}). \quad (2.10)$$

The compressible 3D system can also be formulated by an analogous variable change as a continuity equation coupled with an optimal transport problem [8]. However, in this case the source measure is time-dependent, and the optimal transport between this source measure and the potential vorticity α is to be considered with respect to a non-quadratic cost. Both these elements are new and require significant modifications as well as novel approaches both for the theory and the numerical simulations of the compressible system.

2.2.1. The Source Measure σ_t . Let $\mathcal{X} \subset \mathbb{R}^2$ denote the 2D physical domain of the fluid. The formulation and analysis of the 3D compressible SG system sketched in the previous paragraph motivate the introduction of the quantity $\sigma_t(\mathbf{x}) = \rho(\mathbf{x}, t)\theta(\mathbf{x}, t)$ defined on \mathcal{X} . This quantity plays the role of the source measure in the associated optimal transport problem.

The equation describing the dynamics of σ_t can be obtained by combining Eq. (2.8c) and Eq. (2.8b) as follows

$$\begin{aligned} \rho(D_t\theta + sv) + \theta(D_t\rho + \rho\nabla \cdot \mathbf{u}_S) &= 0 \\ \iff \rho\partial_t\theta + \theta\partial_t\rho &= -\rho\mathbf{u}_S \cdot \nabla\theta - \theta\mathbf{u}_S \cdot \nabla\rho - \rho\theta\nabla \cdot \mathbf{u}_S - \rho sv \\ \iff \rho\partial_t\theta + \theta\partial_t\rho &= -\nabla \cdot (\rho\theta\mathbf{u}_S) - \rho sv \end{aligned}$$

and is given by

$$\partial_t\sigma_t = -\nabla \cdot (\sigma_t\mathbf{u}_S) - \frac{\sigma_t}{\theta}sv. \quad (2.11)$$

We use (2.11) to show that σ_t is a probability measure, provided this is true initially.

Lemma 2.1 (σ_t is a Probability Measure). *Assume at time $t = 0$ that σ_0 is a probability measure. Then σ_t is a probability measure for all t , i.e.*

$$\int_{\mathcal{X}} d\sigma_t(\mathbf{x}) = 1.$$

Proof. Our goal is to show that the time derivative of $\int_{\mathcal{X}} d\sigma_t(\mathbf{x})$ is zero. Note the following relationship

$$\sigma_t\partial_{x_1}(\sigma_t^{\gamma-1}) = (\gamma-1)\sigma_t\sigma_t^{\gamma-2}\partial_{x_1}\sigma_t = \left(\frac{\gamma-1}{\gamma}\right)\partial_{x_1}\sigma_t^\gamma. \quad (2.12)$$

Using the geostrophic balance relation Eq. (2.7) and the equation of state (Eq. (2.1)), the source term in Eq. (2.11), can be rewritten as

$$\frac{\sigma_t}{\theta} s v \stackrel{(2.6)}{=} \frac{s c_p}{f_{\text{cor}}} \sigma_t \partial_{x_1} \Pi \stackrel{(2.1)}{=} \frac{s c_p}{f_{\text{cor}}} \left(\frac{R_d}{p_0} \right)^{\gamma-1} \sigma_t \partial_{x_1} \sigma_t^{\gamma-1} \stackrel{(2.12)}{=} C \partial_{x_1} \sigma_t^\gamma, \quad (2.13)$$

where the constant C is defined as

$$C = \frac{s c_p}{f_{\text{cor}}} \left(\frac{R_d}{p_0} \right)^{\gamma-1} \left(\frac{\gamma-1}{\gamma} \right). \quad (2.14)$$

Thus, the evolution equation for σ_t , Eq. (2.11) can be written as

$$\partial_t \sigma_t + \nabla \cdot (\sigma_t \mathbf{u}_S) = -C \partial_{x_1} \sigma_t^\gamma. \quad (2.15)$$

A direct computation, using the boundary conditions (2.8e) and (2.8f), then shows that

$$\frac{d}{dt} \int_{\mathcal{X}} d\sigma_t(\mathbf{x}) = 0.$$

Therefore σ_t defines a probability measure. \square

2.2.2. The Target Measure α_t . We now consider the transformation to geostrophic variables analogous to the one considered in [14]. For a fixed time t , this is the transformation $T_t : \mathcal{X} \rightarrow \mathcal{Y}$ given by

$$T_t(\mathbf{x}) = \left(x_1 + f_{\text{cor}}^{-1} v(\mathbf{x}, t), \frac{g}{\theta_0 f_{\text{cor}}^2} \theta(\mathbf{x}, t) \right). \quad (2.16)$$

The potential vorticity α_t is the density of the probability measure given by $\alpha_t = (T_t)_\# \sigma_t$, where $\#$ denotes the measure pushforward. In order to derive the PDE for the measure α_t , we first take the material derivative of Eq. (2.16):

$$D_t T_t = \left(D_t x_1 + f_{\text{cor}}^{-1} D_t v \right) = \left(u_1 + s c_p f_{\text{cor}}^{-1} (\Pi - \Pi_0) - u_1, -\frac{sg}{f_{\text{cor}}^2 \theta_0} v \right) = \frac{sg}{f_{\text{cor}} \theta_0} \begin{pmatrix} \frac{c_p \theta_0}{g} (\Pi - \Pi_0) \\ (\mathbf{x} - T_t) \cdot \hat{\mathbf{e}}_1 \end{pmatrix}. \quad (2.17)$$

Define on \mathcal{X} the velocity $\mathbf{W}(\cdot, t)$ as

$$\mathbf{W} := J \begin{pmatrix} (\text{Id} - T_t) \cdot \hat{\mathbf{e}}_1 \\ \frac{c_p \theta_0}{g} (\Pi_0 - \Pi) \end{pmatrix}, \quad (2.18)$$

where

$$J = \frac{sg}{f_{\text{cor}} \theta_0} \begin{pmatrix} 0 & -1 \\ 1 & 0 \end{pmatrix}.$$

Then

$$\partial_t T_t = -\mathbf{u}_S \cdot \nabla T_t + \mathbf{W}.$$

Using the coordinate transformation we can define a new quantity \mathcal{S} , whose value can be extracted from θ and v , as

$$\mathcal{S} := \frac{sv}{\theta} = \frac{sg}{f_{\text{cor}} \theta_0} \frac{(T_t - \text{Id}) \cdot \hat{\mathbf{e}}_1}{T_t \cdot \hat{\mathbf{e}}_3}. \quad (2.19)$$

The weak form of the PDE modelling the dynamics of α_t can now be derived by an explicit computation and, for any test function φ , is given by

$$\frac{d}{dt} \int_{\mathcal{Y}} \varphi(\mathbf{y}) d\alpha_t(\mathbf{y}) = \int_{\mathcal{Y}} \nabla \varphi(\mathbf{y}) \cdot \mathbf{w}(\mathbf{y}, t) d\alpha_t(\mathbf{y}) - \int_{\mathcal{Y}} \varphi(\mathbf{y}) S(\mathbf{y}, t) d\alpha_t(\mathbf{y}), \quad \varphi \in \mathcal{C}_c^\infty(\mathcal{Y}), \quad (2.20)$$

where

$$\mathbf{w}(\mathbf{y}, t) = \mathbf{W}(T_t^{-1}(\mathbf{y}), t) = J \begin{pmatrix} (T_t^{-1}(\mathbf{y}) - \mathbf{y}) \cdot \hat{\mathbf{e}}_1 \\ \frac{c_p \theta_0}{g} (\Pi_0 - \Pi(T_t^{-1}(\mathbf{y}), t)) \end{pmatrix} \quad (2.21)$$

$$S(\mathbf{y}, t) = \mathcal{S}(T_t^{-1}(\mathbf{y}), t) = \frac{sg}{f_{\text{cor}} \theta_0} \frac{(\mathbf{y} - T_t^{-1}(\mathbf{y})) \cdot \hat{\mathbf{e}}_1}{\mathbf{y} \cdot \hat{\mathbf{e}}_3}, \quad (2.22)$$

which are the geostrophic velocity and the source/sink in geostrophic coordinates. We have thus obtained (the weak form of) the forced continuity equation

$$\partial_t \alpha_t + \nabla \cdot (\alpha_t \mathbf{w}) = -\alpha_t S. \quad (2.23)$$

Notice that the vertical component of the geostrophic velocity $\mathbf{w}(\mathbf{y}, t)$, which we denote as $w_3 = \mathbf{w} \cdot \hat{\mathbf{e}}_3$, can be extracted directly from Eq. (2.21) as

$$w_3 = -\frac{sg}{f_{\text{cor}}\theta_0}(\mathbf{y} - T_t^{-1}(\mathbf{y})) \cdot \hat{\mathbf{e}}_1. \quad (2.24)$$

Comparing this expression with Eq. (2.22), we find an exact algebraic relationship between the source term S and the vertical component of the geostrophic velocity,

$$S(\mathbf{y}, t) = -\frac{w_3}{y_3}. \quad (2.25)$$

Substituting this relationship back into Eq. (2.23) yields

$$\partial_t \alpha_t + \nabla \cdot (\alpha_t \mathbf{w}) = \alpha_t \frac{w_3}{y_3}. \quad (2.26)$$

By dividing the entire equation by y_3 and applying the product rule for the divergence operator, we reveal that the forced continuity equation can be rewritten as a homogeneous conservative continuity equation for a modified measure

$$\partial_t \frac{\alpha_t}{y_3} + \nabla \cdot \left(\frac{\alpha_t}{y_3} \mathbf{w} \right) = 0. \quad (2.27)$$

This demonstrates that while the potential vorticity α_t formally contains a source term due to compressibility effects, its evolution is in fact strictly slaved to the geostrophic vertical coordinate.

2.2.3. The Energy Functional and the Optimal Transport Problem. The total geostrophic energy associated to the semi-geostrophic approximation (2.8), namely the sum of kinetic, potential, and internal energy contributions, is given by

$$E_g(t) = \int_{\Omega} \frac{\rho}{2} v^2 + g\rho x_3 - c_p \rho \Pi_0 \theta + c_v \rho \Pi \theta \, d\mathbf{x}, \quad (2.28)$$

by Eq. (2.16), this can be rewritten as

$$\begin{aligned} E_g(t) &= F(T_t, \sigma_t, \alpha_t) \\ &:= \int_{\mathcal{X}} \left(\frac{f_{\text{cor}}^2}{2T_t(\mathbf{x})_3} (x_1 - T_t(\mathbf{x})_1)^2 + g \frac{x_3}{T_t(\mathbf{x})_3} - c_p \Pi_0 \right) \sigma_t \, d\mathbf{x} + \int_{\mathcal{X}} f(\sigma_t(\mathbf{x})) \, d\mathbf{x}, \end{aligned} \quad (2.29)$$

where the dependence of σ_t on α_t has been suppressed for legibility¹ and the internal energy density f is defined by

$$f(s) = \begin{cases} \kappa s^\gamma & \text{if } s \geq 0, \\ \infty & \text{otherwise.} \end{cases} \quad (2.30)$$

The *Cullen convexity principle* states that $F(\cdot, \sigma_t, \alpha_t)$ is minimised over all mass-preserving rearrangements of fluid particles, i.e. that solutions of Eq. (2.8) should also satisfy

$$E_g(t) = \min_{(S_t)_{\#} \sigma_t = \alpha_t} F(S_t, \sigma_t, \alpha_t). \quad (2.31)$$

This can be written in terms of optimal transport as

$$E_g(t) = \mathcal{T}_c(\sigma_t, \alpha_t) + \int_{\mathcal{X}} f(\sigma_t) \, d\mathbf{x} =: E(\sigma_t, \alpha_t),$$

¹See [5] for full details on the relationship between the source measure, the energy, and the target measure.

where \mathcal{T}_c , defined in (2.10), is the solution to an optimal transport problem with respect to the cost defined as

$$c(\mathbf{x}, \mathbf{y}) = \frac{f_{\text{cor}}^2}{2y_3}(x_1 - y_1)^2 + g \frac{x_3}{y_3} - c_p \Pi_0. \quad (2.32)$$

2.3. Semi-discrete optimal transport. We now introduce a discretisation of the of PDE (2.27) by using the template of semi-discrete optimal transport. Namely, we consider a set of points $\mathbf{z}_t \in \mathcal{Y}$ and define a particle approximation of the potential vorticity α_t for fixed t

$$\alpha_t^N(\mathbf{z}) = \sum_{i=1}^N m_t^i \delta_{\mathbf{z}_t^i}. \quad (2.33)$$

As was done in [14], to which we refer for details, we now use ideas of semi-discrete optimal transport. Given a discrete target measure such as α_t^N , the optimal transport map with respect to the cost $c(\mathbf{x}, \mathbf{y})$ becomes an optimal tessellation of \mathcal{X} , called a c -Laguerre tessellation. Let the set of *seed vectors* be given by

$$D^N := \left\{ \mathbf{z} = (\mathbf{z}^1, \dots, \mathbf{z}^N) \in \mathcal{Y}^N : z_3^i \neq z_3^j \text{ whenever } i \neq j \right\}, \quad (2.34)$$

and the set of admissible mass given by

$$\Delta^N := \left\{ \mathbf{m} = (m^1, \dots, m^N) \in (0, 1]^N : \sum_{i=1}^N m^i = 1 \right\}. \quad (2.35)$$

The barycenters of the cells in this tessellation are known as the centroids, \mathbf{C}^i .

Definition 2.1 (c -Laguerre tessellation). Given $(\mathbf{w}, \mathbf{z}) \in \mathbb{R}^N \times D^N$, the c -Laguerre tessellation of \mathcal{X} generated by (\mathbf{w}, \mathbf{z}) is the collection of Laguerre cells $\{\mathcal{L}\}_{i=1}^N$ defined by

$$\mathcal{L} := \left\{ \mathbf{x} \in \mathcal{X} : c(\mathbf{x}, \mathbf{z}^i) - w^i \leq c(\mathbf{x}, \mathbf{z}^j) - w^j \forall j \in \{1, \dots, N\} \right\}, \quad i \in \{1, \dots, N\}.$$

Definition 2.2 (Centroid map). Given $\mathbf{m} \in \Delta^N$ and a source measure $\sigma \in \mathcal{P}_{\text{ac}}(\mathcal{X})$, define the centroid map $\mathbf{C} : D^N \times \Delta^N \rightarrow (\mathbb{R}^3)^N$ by $\mathbf{C}(\mathbf{z}) := (\mathbf{C}^1(\mathbf{z}), \dots, \mathbf{C}^N(\mathbf{z}))$, where

$$\mathbf{C}^i(\mathbf{z}, \mathbf{m}) := \frac{1}{m^i} \int_{L_c^i(\mathbf{w}_*(\mathbf{z}, \mathbf{m}), \mathbf{z})} \mathbf{x} \, d\sigma(\mathbf{x}). \quad (2.36)$$

For clarity the dependence on the mass will be suppressed.

This says that $\mathbf{C}^i(\mathbf{z})$ is the centroid (or barycentre) of the set of points $T_{\alpha^N}^{-1}(\{\mathbf{z}^i\})$ transported to \mathbf{z}^i in the optimal transport from σ to α^N for the cost c .

PDE Discretisation. Starting with the velocity term on the right-hand side of Eq. (2.20) we can write

$$\int_{\mathcal{Y}} \nabla \varphi(\mathbf{y}) \cdot \mathbf{w}(\mathbf{y}, t) \, d\alpha_t(\mathbf{y}) = \sum_{i=1}^N m_t^i \nabla \varphi(\mathbf{z}_t^i) \cdot J \left(\begin{array}{c} (\mathbf{C}^i(\mathbf{z}_t) - \mathbf{z}_t^i) \cdot \hat{\mathbf{e}}_1 \\ \frac{c_p \theta_0}{g} E_I(\mathbf{z}_t, \mathbf{m}_t) \end{array} \right), \quad (2.37)$$

where

$$E_I(\mathbf{z}_t, \mathbf{m}_t) := \frac{1}{m_t^i} \int_{L_c^i(\mathbf{w}(\mathbf{z}_t, \mathbf{m}_t), \mathbf{z}_t)} \Pi_0 - \Pi(\mathbf{x}) \, d\sigma_t(\mathbf{x}). \quad (2.38)$$

The source/sink term gives

$$\int_{\mathcal{Y}} \varphi(\mathbf{y}) S(\mathbf{y}, t) \, d\alpha_t(\mathbf{y}) = \sum_{i=1}^N m_t^i \varphi(\mathbf{z}_t^i) \frac{(\mathbf{z}_t^i - \mathbf{C}^i(\mathbf{z}_t)) \cdot \hat{\mathbf{e}}_1}{\mathbf{z}_t^i \cdot \hat{\mathbf{e}}_3}. \quad (2.39)$$

The left-hand side of Eq. (2.20) yields

$$\frac{d}{dt} \int_{\mathcal{Y}} \varphi(\mathbf{y}) \, d\alpha_t(\mathbf{y}) = \sum_{i=1}^N \left[\dot{m}_t^i \varphi(\mathbf{z}_t^i) + m_t^i \nabla \varphi(\mathbf{z}_t^i) \cdot \dot{\mathbf{z}}_t^i \right]. \quad (2.40)$$

Combining equations (2.37), (2.39), and (2.40) gives

$$\begin{aligned} & \sum_{i=1}^N \left[\dot{m}_t^i \varphi(\mathbf{z}_t^i) + m_t^i \nabla \varphi(\mathbf{z}_t^i) \cdot \dot{\mathbf{z}}_t^i \right] \\ &= \sum_{i=1}^N m_t^i \nabla \varphi(\mathbf{z}_t^i) \cdot J \left(\frac{(\mathbf{C}^i(\mathbf{z}_t) - \mathbf{z}_t^i) \cdot \hat{\mathbf{e}}_1}{\frac{c_p \theta_0}{g} E_I(\mathbf{z}_t, \mathbf{m}_t)} \right) - \sum_{i=1}^N m_t^i \varphi(\mathbf{z}_t^i) \frac{(\mathbf{z}_t^i - \mathbf{C}^i(\mathbf{z}_t)) \cdot \hat{\mathbf{e}}_1}{\mathbf{z}_t^i \cdot \hat{\mathbf{e}}_3}. \end{aligned} \quad (2.41)$$

Fix i . First choose φ such that $\varphi(\mathbf{z}_t^i) = 1$, $\varphi(\mathbf{z}_t^j) = 0$ for all $j \neq i$ and φ constant in a neighbourhood of \mathbf{z}_t^k for all k . This gives an ODE for m^i . Then choosing φ to be a constant in a neighbourhood of \mathbf{z}_t^j for all $j \neq i$ implies that $\nabla \varphi = 0$ in a neighbourhood of \mathbf{z}_t^j and taking φ such that $\nabla \varphi(\mathbf{y}) = \mathbf{y}$ in a neighbourhood of \mathbf{z}_t^i then gives an ODE for \mathbf{z}^i . The evolution of the i -th particle, for $i \in \{1, \dots, N\}$, is governed by the coupled ordinary differential equations:

$$\begin{cases} \dot{\mathbf{z}}_t^i = J \mathbf{w}^i(t), \\ \dot{m}_t^i = -m_t^i S^i(t), \end{cases} \quad (2.42)$$

where

$$\begin{aligned} \mathbf{w}^i(t) &= \left(\frac{(\mathbf{C}^i(\mathbf{z}_t) - \mathbf{z}_t^i) \cdot \hat{\mathbf{e}}_1}{\frac{c_p \theta_0}{g} E_I(\mathbf{z}_t, \mathbf{m}_t)} \right), \\ S^i(t) &= \frac{sg}{f_{\text{cor}} \theta_0} \frac{(\mathbf{z}_t^i - \mathbf{C}^i(\mathbf{z}_t)) \cdot \hat{\mathbf{e}}_1}{\mathbf{z}_t^i \cdot \hat{\mathbf{e}}_3}. \end{aligned}$$

However, as observed in the continuous formulation, this system contains an exact cancellation. From the definition of J , the vertical velocity of the i -th particle is explicitly

$$\dot{z}_{t,3}^i = \frac{sg}{f_{\text{cor}} \theta_0} (\mathbf{z}_t^i - \mathbf{C}^i(\mathbf{z}_t)) \cdot \hat{\mathbf{e}}_1. \quad (2.43)$$

Comparing this to the source term $S^i(t)$, we find the discrete analogue of the relationship derived in the continuous section

$$S^i(t) = -\frac{\dot{z}_{t,3}^i}{z_{t,3}^i}. \quad (2.44)$$

Substituting this directly into the mass evolution equation gives:

$$\dot{m}_t^i = m_t^i \frac{\dot{z}_{t,3}^i}{z_{t,3}^i} \implies \frac{\dot{m}_t^i}{m_t^i} = \frac{\dot{z}_{t,3}^i}{z_{t,3}^i}. \quad (2.45)$$

Integrating this expression reveals an exact algebraic relationship between the mass of the i -th cell and its vertical position:

$$m_t^i = m_0^i \frac{z_{t,3}^i}{z_{0,3}^i}. \quad (2.46)$$

Therefore, the dynamic evolution of the system is completely determined by the ordinary differential equations for the particle positions $z_{t,3}^i$, with the cell masses m_t^i evolving proportionally to their vertical coordinates. This fundamentally differs from the incompressible cases, where the masses m_i are constant in time.

3. NUMERICAL METHOD

In this section we describe the numerical implementation of this 2D slice model. The numerical simulation of the solutions of the ODE system (2.42) constitutes the first step towards a full 3D discretisation scheme for the compressible semi-geostrophic system.

3.1. Optimal Transport Framework. The discretisation derived in Section 2 reduces the evolution of the atmosphere to a system of ODEs, Eq. (2.42) governing the particle positions \mathbf{z}^i , while the masses m^i are updated exactly at each timestep through their algebraic dependence on the vertical coordinate. However, evaluating the driving vector fields, specifically the centroids \mathbf{C}^i and internal energy terms E_I , requires the computation of the exact c -Laguerre tessellation at every timestep.

While particle positions \mathbf{z} are known from the time-integration, the weights $\mathbf{w} \in \mathbb{R}^N$ defining the cells are implicit. They must be uniquely determined to satisfy the mass consistency condition required by the particle approximation

$$\mathcal{M}^i(\mathbf{w}) := \int_{L_c^i(\mathbf{w}_*, \mathbf{z})} d\sigma = m^i, \quad \forall i = 1, \dots, N. \quad (3.1)$$

Finding the weights that satisfy Eq. (3.1) is equivalent to solving the dual formulation of the semi-discrete optimal transport problem. We recover the optimal weights \mathbf{w}_* by maximizing the Kantorovich dual function

$$\mathcal{G}(\mathbf{w}, \mathbf{z}) = \sum_{i=1}^N w^i m^i - \int_{L_c^i(\mathbf{w}, \mathbf{z})} f^*(w^i - c(\mathbf{x}, \mathbf{z}^i)) d\mathbf{x}. \quad (3.2)$$

The functional \mathcal{G} is concave and smooth, allowing us to solve for \mathbf{w}_* efficiently using a damped Newton algorithm. The gradient of this functional is exactly the mass mismatch error,

$$\nabla_{\mathbf{w}} \mathcal{G} = m^i - \mathcal{M}^i, \quad (3.3)$$

while its Hessian is determined by the geometric interactions between adjacent cells (see Appendix A and [5]).

In the compressible setting, this problem is computationally demanding because the source measure σ is non-uniform and evolves in time, while in addition the cost function is non-quadratic. To compute the necessary integrals for the gradient and Hessian efficiently, we exploit the specific geometry of the cost function, as detailed in the following section.

3.2. Geometry of the Cost Function. The efficient minimisation of the dual functional \mathcal{G} requires computing integrals over the Laguerre cells. Due to the form of the cost function, the boundaries of these cells are segments of curved surfaces, making construction of the tessellation computationally expensive and integration over the cells expensive and geometrically complex.

To simplify the problem, we map the computation into a coordinate system where the cell boundaries become linear. For a fixed $\mathbf{y} \in \mathcal{Y}$, define the diffeomorphism

$$\Phi = \Phi(\cdot, \mathbf{y}) : \mathbb{R}^2 \rightarrow \mathbb{R}^2 \quad (3.4)$$

called the *c-exponential map* (see [12, Remark 4.4]), by

$$\Phi(\mathbf{x}; \mathbf{y}) := \exp_{\mathbf{y}}^c(\mathbf{x}) = (-D_{\mathbf{y}} c(\cdot, \mathbf{y}))^{-1}(\mathbf{x}), \quad (3.5)$$

which explicitly can be written as

$$\Phi(\mathbf{x}; \mathbf{y}) = \begin{pmatrix} \frac{y_3}{f_{\text{cor}}^2} x_1 + y_1 \\ \frac{y_3^2}{g} \left(x_3 - \frac{x_1^2}{2f_{\text{cor}}^2} \right) \end{pmatrix}. \quad (3.6)$$

This change of variables simplifies the geometric structure of the problem significantly. Specifically, we show that the cost function satisfies the so-called *Loeper's condition* [12], which ensures that the cells are convex in the transformed coordinates.

Lemma 3.1 (Loeper's condition). *Given any $\mathbf{y}, \mathbf{z} \in \mathcal{Y}$, define $u : \mathbb{R}^2 \rightarrow \mathbb{R}$ by*

$$u(\mathbf{x}) = c(\Phi(\mathbf{x}; \mathbf{y}), \mathbf{y}) - c(\Phi(\mathbf{x}; \mathbf{y}), \mathbf{z}).$$

Then u is affine. In particular, u is convex, and hence the 2D compressible semi-geostrophic cost function c satisfies Loeper's condition.

Proof. First we compute that, for all $\mathbf{x} \in \mathbb{R}^2$,

$$c(\Phi(\mathbf{x}; \mathbf{y}), \mathbf{y}) = \frac{1}{y_3} \left(\frac{f_{\text{cor}}^2}{2} (\Phi_1(\mathbf{x}; \mathbf{y}) - y_1)^2 + g\Phi_2(\mathbf{x}; \mathbf{y}) \right) - c_p\Pi_0 = y_3x_3 - c_p\Pi_0.$$

Similarly,

$$\begin{aligned} c(\Phi(\mathbf{x}; \mathbf{y}), \mathbf{z}) &= \frac{1}{z_3} \left(\frac{f_{\text{cor}}^2}{2} (\Phi_1(\mathbf{x}; \mathbf{y}) - z_1)^2 + g\Phi_2(\mathbf{x}; \mathbf{y}) \right) - c_p\Pi_0 \\ &= \frac{f_{\text{cor}}^2}{2z_3} \left(\frac{y_3}{f_{\text{cor}}^2} x_1 + y_1 - z_1 \right)^2 + \frac{g}{z_3} \left(\frac{y_3^2}{g} \left(x_3 - \frac{x_1^2}{2f_{\text{cor}}^2} \right) \right) - c_p\Pi_0 \\ &= \frac{f_{\text{cor}}^2}{2z_3} (y_1 - z_1)^2 + \frac{y_3^2}{z_3} x_3 + \frac{y_3x_1}{z_3} (y_1 - z_1) - c_p\Pi_0. \end{aligned}$$

Therefore u is affine, as required. \square

This result has a crucial practical implication. In the coordinate system defined by Φ , the Laguerre cell is a convex polygon defined by the intersection of half planes (for the 3D analogue see [5]). This allows us to employ efficient computational geometry algorithms, specifically half-plane clipping, to compute the volume and moments required by the Newton solver.

Note that, a priori, the periodicity in the x_1 -direction complicates the construction of the tessellation. However, in the x_1 direction the cost function is the standard quadratic cost. Hence the results of [4] can be applied without substantial modification, while taking into account, in determining the correct periodic tessellation, that the c -exponential chart is not a periodic transformation.

In practice, computing the integrals for the dual functional and its derivatives relies on this transformation. As detailed in Appendix A, we map the computation into a single c -exponential chart defined around a reference point $y = [0, 1]^T$. Within this chart, the Laguerre cells form convex polygons, allowing us to use the divergence theorem to reduce the required 2D volume integrals to 1D boundary line integrals. This avoids expensive quadrature over the cell in favour of line integrals yielding cheap and accurate gradients and Hessians used in our Newton solver. Furthermore, we also visualize the tessellations directly within this transformed coordinate system. This is why the physically rectangular domain appears to have curved boundaries in Figure 3. The transformation renders the complex parabolic cell boundaries as straight-edged polygons, simultaneously warping the global domain. For more detailed discussions of c -exponential charts and their use for semi-discrete optimal transport methods for the semi-geostrophic equations see [5, 14].

3.3. Non-Dimensionalisation. To non-dimensionalise the ODE in Eq. (2.42), we introduce dimensionless variables, marked with tildes, using the following scalings :

$$\begin{aligned} t &= \frac{f_{\text{cor}}\theta_0}{sg} \tilde{t}, \\ x_1 &= L_0\tilde{x}_1, \\ x_2 &= H_1\tilde{x}_2, \\ z_1^i &= L_0\tilde{z}_1^i, \\ z_2^i &= H_2\tilde{z}_2^i. \end{aligned}$$

Here, L_0 denotes the horizontal reference scale. We utilize two distance vertical reference scales H_1 for the physical height and H_2 for the geostrophic vertical coordinate, which accounts for the thermodynamic scaling inherent in the coordinate transformation. Substituting these relations into the cost function we obtain

$$c(\tilde{\mathbf{x}}, \tilde{\mathbf{z}}^i) = \frac{1}{H_2\tilde{z}_2^i} \left(\frac{f_{\text{cor}}^2}{2} L_0^2 (\tilde{x}_1 - \tilde{z}_1^i)^2 + gH_1\tilde{x}_2 \right) - c_p\Pi_0$$

$$= \frac{f_{\text{cor}}^2 L_0^2}{2H_2 \tilde{z}_2^i} (\tilde{x}_1 - \tilde{z}_1^i)^2 + \frac{gH_1 \tilde{x}_2}{H_2 \tilde{z}_2^i} - c_p \Pi_0.$$

Defining the non-dimensional parameters

$$F = \sqrt{\frac{f_{\text{cor}}^2 L_0^2}{H_2}}, \quad (3.7)$$

$$G = \frac{gH_1}{H_2}, \quad (3.8)$$

the cost function becomes

$$c(\tilde{\mathbf{x}}, \tilde{\mathbf{z}}^i) = \frac{F^2}{2\tilde{z}_2^i} (\tilde{x}_1 - \tilde{z}_1^i)^2 + G \frac{\tilde{x}_2}{\tilde{z}_2^i} - c_p \Pi_0. \quad (3.9)$$

In our simulations, we select the reference scales $L_0 = 10^7 \text{m}$, $H_1 = 10^5 \text{m}$, and $H_2 = 10^6 \text{m}$. These choices result in unity parameters $F = 1$ and $G = 1$, significantly simplifying the implementation. Note that these reference scales differ from the physical boundaries L and H defined in Table 1.

The non-dimensional form of the particle evolution system Eq. (2.42) (ignoring the mass ODE as we showed that it is slaved to the particle positoin) is given by

$$\begin{cases} \dot{\tilde{z}}_1^i = \frac{\alpha}{m^i} \int_{L_t^i(\mathbf{w}, \mathbf{z})} \Pi(\mathbf{x}) - \Pi_0 d\sigma_t^i(\mathbf{x}), \\ \dot{\tilde{z}}_2^i = \beta (\tilde{C}_1^i - \tilde{z}_1^i), \end{cases} \quad (3.10)$$

where the dimensionless coupling constants α and β are given by :

$$\alpha = \frac{c_p \theta_0}{L_0 g} \quad \text{and} \quad \beta = \frac{L_0}{H_2}. \quad (3.11)$$

3.4. Description of the Numerical Algorithm. Our numerical scheme follows and extends the semi-discrete framework developed for incompressible flows outlined in [9, 15] to the compressible setting. The algorithm evolves the discrete particle system by splitting the problem into two distinct phases at each timestep. A geometric construction phase, i.e. solving the optimal transport problem, and a dynamic evolution phase, i.e. integrating the ODES.

The procedure for advancing the system from time t_n to $t_{n+1} = t_n + \Delta t$ is detailed below.

Step 1 : Optimal Transport. At time t_n , the particle positions \mathbf{z} and the masses m are fixed. To evaluate the driving vector fields, we must first construct the Laguerre tessellation that satisfies the mass constraint. Using a damped Newton solver we recover the unique optimal weights \mathbf{w}_* by maximising the dual functional \mathcal{G} given in (3.2). We use a rescaling algorithm suggested by [16] to initialise the solver and accelerate convergence. For each Newton iteration, the Laguerre cells are constructed in the c -exponential charts introduced in Section 3.2. In these local coordinates, the cells are convex polygons, allowing for robust construction via half-plane intersection algorithms.

Step 2 : Integral Evaluation. A central challenge in this scheme is the accurate computation of the integrals defining the gradient and Hessian of \mathcal{G} , the centroids, and internal energy. Since the cells are polygonal in the c -exponential charts, we avoid expensive quadrature by converting area integrals into boundary line integrals where possible using the divergence theorem, see Appendix A.

Step 3 : Dynamic Evolution. Once the optimal weights \mathbf{w}_* and the corresponding cells are established, we evaluate the non-dimensional velocity fields from Eq. (3.10). We then advance the particle state using a standard explicit Adams-Bashforth scheme (AB2). Crucially, the particle masses m^i are not integrated numerically. Instead, they are updated exactly at each

timestep using the algebraic constraint

$$m^i(t) = m^i(0) \frac{z_2^i(t)}{z_2^i(0)}, \quad (3.12)$$

derived in Section 2.3. At first glance, the presence of a source term in the governing PDE (Eq. (2.23)) suggests that a fully compressible scheme would require integrating a third coupled ODE for the mass evolution, which inherently risks the accumulation of numerical drift. By exploiting this exact analytical relationship, our algorithm completely bypasses the numerical integration of a mass equation. This ensures mass conservation and prevents accumulation of numerical errors associated with the mass evolution.

This approach using the optimal transport solver naturally preserves the global conservation properties of the system while capturing the compressibility effects unique to this model.

4. NUMERICAL EXPERIMENTS

In this section, we validate our numerical algorithm and demonstrate its capability to simulate compressible atmospheric dynamics. We begin by defining the experimental configuration, including the physical parameters and initial conditions used in our simulations. We then present a benchmark study based on an analytical single-seed solution to quantify error convergence, followed by full-scale simulations of frontogenesis.

4.1. Experimental Setup. Our simulations follow the vertical slice frontogenesis test case adapted from [18]. The physical domain is a periodic channel in the horizontal direction x_1 with rigid boundaries at the top and bottom.

4.1.1. Parameters. We adopt the parameter choices listed in Table 1, which correspond to realistic atmospheric scales. In addition to these dimensional values, the initial condition is characterised by the non-dimensional Burger number $Bu = 0.5$ and the amplitude parameter $a = -7.5$.

Parameter	Value	Unit
L	10^6	m
H	10^4	m
f_{cor}	10^{-4}	s^{-1}
N	5×10^{-3}	s^{-1}
g	10	m s^{-2}
p_0	10^5	$\text{kg m}^{-1} \text{s}^{-2}$
θ_0	300	K
s	-3×10^{-6}	K m^{-1}
c_p	1003.5	$\text{m}^2 \text{K}^{-1} \text{s}^{-2}$
R_d	287.052874	$\text{m}^2 \text{K}^{-1} \text{s}^{-2}$

TABLE 1. Physical parameters used in the numerical simulations of compressible frontogenesis.

4.1.2. Initial Conditions. The initial state is defined by a hydrostatic base state perturbed to induce frontogenesis. Recall from Eq. (2.5) that the total potential temperature Θ is decomposed into a reference value, a background vertical profile, and a time-dependent perturbation

$$\Theta(\mathbf{x}, t) = \theta_0 + \bar{\theta}(x_2) + \theta(x_1, x_3, t). \quad (4.1)$$

The in-slice potential temperature θ is further split into a hydrostatic base state $\bar{\theta}(x_3)$ and a perturbation $\tilde{\theta}(x_1, x_3)$

$$\theta(x_1, x_3) = \bar{\theta}(x_3) + \tilde{\theta}(x_1, x_3). \quad (4.2)$$

The base state is stratified according to the Brunt-Väisälä frequency N

$$\bar{\theta}(x_3) = \theta_0 \exp\left(\frac{N^2}{g}\left(x_3 - \frac{H}{2}\right)\right). \quad (4.3)$$

To trigger the dynamics, we impose the following perturbation

$$\tilde{\theta}(x_1, x_3) = \frac{\theta_0 a N}{g} \left(-\left(1 - \frac{\text{Bu}}{2} \coth \frac{\text{Bu}}{2}\right) \sinh Z(x_3) \cos \frac{\pi x_1}{L} - n \text{Bu} \cosh Z(x_3) \sin \frac{\pi x_1}{L} \right), \quad (4.4)$$

where the vertical coordinate is scaled as

$$Z(x_3) = \text{Bu} \left(\frac{x_3}{H} - \frac{1}{2} \right), \quad (4.5)$$

and the normalisation constant n is given by

$$n = \frac{1}{\text{Bu}} \left(\left(\frac{\text{Bu}}{2} - \tanh \frac{\text{Bu}}{2} \right) \left(\coth \frac{\text{Bu}}{2} - \frac{\text{Bu}}{2} \right) \right)^{\frac{1}{2}}. \quad (4.6)$$

Finally, the initial particle distribution is determined by the transport map $T_0(\mathbf{x})$, which maps the physical coordinates to geostrophic coordinates. This map depends on the meridional velocity v , derived from the Exner pressure Π via the hydrostatic balance relation

$$T(\mathbf{x}, t) = \left(x_1 + \frac{f_{\text{cor}}^{-1} v(\mathbf{x}, t)}{\frac{g \theta(\mathbf{x}, t)}{f_{\text{cor}}^2 \theta_0}} \right). \quad (4.7)$$

4.2. Validation: Single Seed Benchmark. To establish a foundational test case and validate the accuracy of our integral computations, we consider a first benchmark problem consisting of a single particle seed. Unlike the full simulation, this scenario admits an analytical solution, providing a rigorous ground truth for verifying our numerical implementation.

For this specific benchmark, we adopt the following simplified set of non-dimensional parameters

$$N = c_p = \theta_0 = s = R_d = p_0 = \Pi_0 = f_{\text{cor}} = g = 1, \quad \gamma = 2, \quad \kappa = \frac{1}{2}. \quad (4.8)$$

The computational domain is a two-dimensional box, periodic in the horizontal direction, defined as

$$\mathcal{X} = (-1, 1] \times [0, 1]. \quad (4.9)$$

In this setting, the optimal weight w_* for the single Laguerre cell is determined solely by the mass constraint, which requires the total mass of the cell to integrate to one. This leads to the integral equation

$$1 = \int_{L_c^i(w, \mathbf{z})} f'(w - c(\mathbf{x}, \mathbf{z})) \, d\mathbf{x}, \quad (4.10)$$

for $\mathbf{x} = (x_1, x_2)^T$ and $\mathbf{z} = (z_1, z_2)^T$. Solving this equation yields the optimal weight w_* as a function of the particle's vertical position z_2 .

To solve for the optimal weight w_* , we first define the function $p(w, z_2)$

$$\begin{aligned} p(w, z_2) = & \frac{1}{60z_2} \left(3 - 32\sqrt{2}\sqrt{wz_2 + z_2 - 1} \right. \\ & - 4(w+1)z_2 \left(-16\sqrt{2}\sqrt{wz_2 + z_2 - 1} \right. \\ & \left. \left. + (w+1)z_2 \left(8\sqrt{2}\sqrt{wz_2 + z_2 - 1} - 15 \right) + 5 \right) \right). \end{aligned} \quad (4.11)$$

By solving Equation (4.10), we obtain the optimal weight w_* as a piecewise function of the particle's vertical position, z_2

$$w_* = \begin{cases} \frac{1}{6z_2}(4 - 3z_2) & \text{if } z_2 \geq \frac{5}{3}, \\ \frac{1 - 6z_2 + 6\sqrt{z_2 - \frac{1}{45}}}{6z_2} & \text{if } \frac{1}{45} \leq z_2 \leq \frac{43}{60}, \\ \text{The solution to } 1 = p(w, z_2) & \text{otherwise.} \end{cases} \quad (4.12)$$

Optimal Weight w_* as a Function of Particle Height z_2

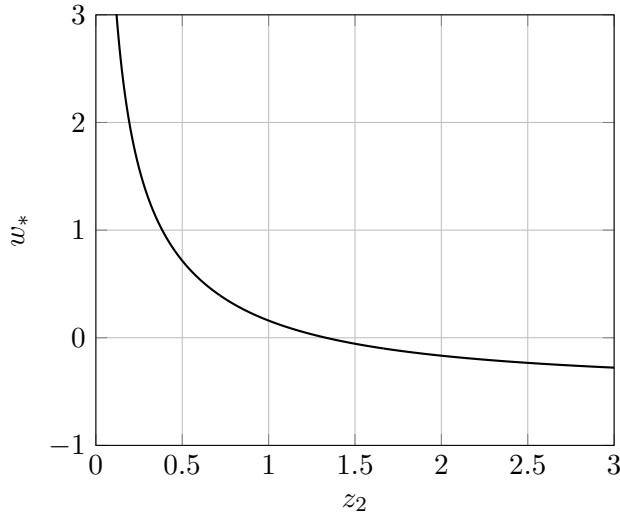


FIGURE 1. The optimal weight w_* derived from the integral, plotted as a function of the parameter z_2 .

The relationship between the optimal weight w_* and the particle's height z_2 is visualized in Figure 1.

With the optimal weight determined, we can analytically evaluate the derived quantities. The first component of the centroid of the Laguerre cell, C_1 , simplifies elegantly due to the symmetry of the domain and the cost function. With the change of variables, $u = x_1 - z_1$,

$$C_1 = \int_{L_c^i(w_*, \mathbf{z})} x_1 f'(w_* - c(\mathbf{x}, \mathbf{z})) \, d\mathbf{x} = \int_0^1 \int_{z_1-1}^{z_1+1} x_1 f'(w_* - c(\mathbf{x}, \mathbf{z})) \, d\mathbf{x} \quad (4.13)$$

$$= \int_0^1 \int_{-1}^1 (u + z_1) f' \left(w_* - \frac{1}{z_2} \left(\frac{1}{2} u^2 + x_2 \right) + 1 \right) \, du dx_2 \quad (4.14)$$

$$= \int_{L_c^i(w_*, \mathbf{z})} \underbrace{u f' \left(w_* - \frac{1}{z_2} \left(\frac{1}{2} u^2 + x_2 \right) + 1 \right)}_{\substack{\text{odd function in } u \\ \text{over symmetric domain } [-1,1]}} \, du dx_2 \quad (4.15)$$

$$+ z_1 \int_{L_c^i(w_*, \mathbf{z})} f' \left(w_* - \frac{1}{z_2} \left(\frac{1}{2} u^2 + x_2 \right) + 1 \right) \, du dx_2 \quad (4.16)$$

$$= 0 + z_1 = z_1. \quad (4.17)$$

The integral of the odd function over a symmetric domain vanishes, resulting in the first component of the centroid simply being the particle's horizontal position, z_1 . Referring back to our non-dimensional ODEs (Eq. (3.10)), this equality immediately implies that the vertical velocity of the particle is zero. Consequently, through our exact algebraic mass-height relationship, the mass of the particle remains perfectly constant, which is exactly required for a single-seed system holding the total domain mass. Next, we evaluate the internal energy contribution, E_I , which is defined as

$$E_I = \int_{L_c^i(w_*, \mathbf{z})} f'(w_* - c(\mathbf{x}, \mathbf{z})) - f'(w_* - c(\mathbf{x}, \mathbf{z}))^2 \, d\mathbf{x} \quad (4.18)$$

$$= 1 - \int_{L_c^i(w_*, \mathbf{z})} f'(w_* - c(\mathbf{x}, \mathbf{z}))^2 \, d\mathbf{x}. \quad (4.19)$$

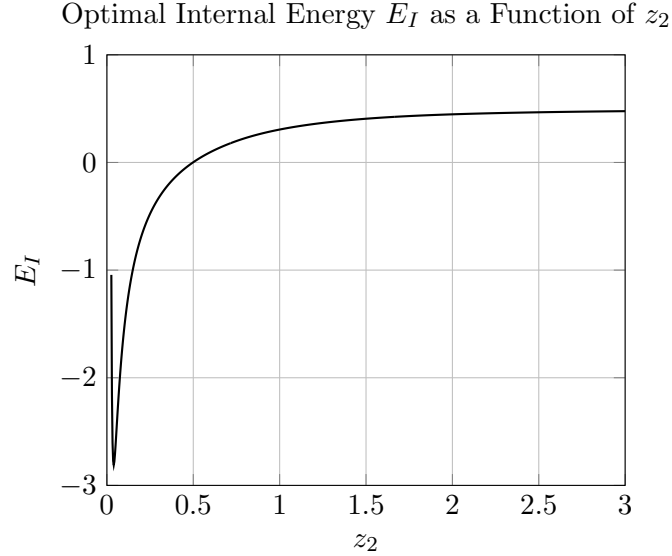


FIGURE 2. The optimal internal energy E_I as a function of the parameter z_2 .

To express the internal energy as a function of z_2 , we introduce the function $q(w_*, z_2)$

$$\begin{aligned}
q(w_*, z_2) = 1 - \frac{1}{420z_2^2} & \left(128\sqrt{2}\sqrt{w_*z_2 + z_2 - 1} \right. \\
& - 2(w_* + 1)z_2 \left(3 \left(64\sqrt{2}\sqrt{w_*z_2 + z_2 - 1} - 7 \right) \right. \\
& \left. \left. + 2(w_* + 1)z_2 \left(-96\sqrt{2}\sqrt{w_*z_2 + z_2 - 1} \right. \right. \right. \\
& \left. \left. \left. + 2(w_* + 1)z_2 \left(16\sqrt{2}\sqrt{w_*z_2 + z_2 - 1} - 35 \right) + 35 \right) \right) - 5 \right).
\end{aligned} \tag{4.20}$$

Similar to the optimal weight, the internal energy E_I is a piecewise function of z_2

$$E_I = \begin{cases} \frac{1}{2} - \frac{19}{90z_2^2} & \text{if } z_2 \geq \frac{5}{3}, \\ 1 - \frac{630z_2\sqrt{225z_2-5}+28\sqrt{225z_2-5}-20}{14175z_2^2} & \text{if } \frac{1}{45} \leq z_2 \leq \frac{43}{60}, \\ q(w_*, z_2), \text{ where } w_* \text{ solves } 1 = p(w, z_2) & \text{otherwise.} \end{cases} \tag{4.21}$$

Figure 2 plots the internal energy E_I as a function of the particle's height z_2 . This analysis simplifies the governing ODE system to a trivial trajectory

$$\begin{cases} \dot{z}_1 = E_I(z_2), \\ \dot{z}_2 = 0, \end{cases} \tag{4.22}$$

which implies the particles moves horizontally with a constant velocity determined by its fixed height. Given an initial condition $\bar{\mathbf{z}} = \mathbf{z}_0$, the trajectory is given by

$$\mathbf{z}_t = (E_I(\bar{z}_2)t + \bar{z}_1)\hat{\mathbf{e}}_1. \tag{4.23}$$

This analytical solution for the particle's path in the single seed benchmark provides a crucial tool for validating our numerical methods. By comparing the output of our numerical simulations against this exact solution, we confirmed that our algorithms for cell construction and integral evaluation are functioning correctly and producing accurate values.

4.3. Simulation Results.

4.3.1. *Full Simulation Dynamics.* The evolution of the compressible frontogenesis test case is visualized in Figure 3. The figure displays snapshots of the particles positions alongside the interpolated Eulerian fields for velocity, potential temperature, and mass density at days 2, 4, 7, and 11.

Qualitatively, our results capture the standard lifecycle of the baroclinic instability, exhibiting excellent agreement with the structural evolution reported in the reference finite-element solutions. However, a notable difference in our simulation is the significant horizontal propagation or drift of the frontal system.

This lateral motion arises from our treatment of the reference Exner pressure constant, Π_0 . In the reference study [18], Π_0 is tuned specifically to minimize the mean horizontal wind and centre the front within the domain. In contrast, our method strictly adheres to the physical definition given in Eq. (2.9), where Π_0 is the initial spatial average of the Exner pressure. Consequently, our solution retains a non-zero mean geostrophic flow. This results in the front drifting across the periodic domain and appearing more elongated due to the shearing effect of the background mean flow.

The dynamics proceed through distinct phases. The system begins with a broad, gentle wave structure characteristic of linear normal mode. The particle distribution remains relatively uniform, though initial displacements are visible. The instability then matures into a sharp frontal discontinuity. The Lagrangian nature of our scheme is most evident here, as the particle positions clearly show clustering in the zone of the front, naturally adapting the effective resolution of the region of highest gradients.

The coupling of the potential temperature and mass fields reveals the coherent thermodynamic structure of the frontal circulation. By viewing these fields in tandem, we observe a strong correlation between the warm sector and regions of mass accumulation at the upper boundary. Physically, this is consistent with the vertical transport inherent in baroclinic instability: buoyant warm air rises and is effectively compressed against the rigid upper lid, resulting in the observed local mass increase. Conversely, the cold sector near the surface is associated with lower mass, consistent with the sinking and spreading of denser air. This suggests that the compressible formulation successfully captures the asymmetric density response of the rising warm air versus the sinking cold air.

4.3.2. *Conservation Properties.* To quantify the conservation properties of the numerical scheme, we compute the relative error normalized by the mean value of the quantity over the simulation. For a generic quantity Q , the time-dependent error is defined as

$$\text{Error}(t) = \frac{Q_{\text{mean}} - Q(t)}{Q_{\text{mean}}}. \quad (4.24)$$

Figure 4 displays the relative error in the total geostrophic energy, $E_g(t)$. While the continuous semi-geostrophic system formally conserves this energy, our fully discrete scheme introduces a temporal discretization error via the explicit Adams-Bashforth integration. The plot shows that this relative error remains small and bounded, verifying the stability of the time-stepping scheme even as the flow develops sharp gradients during the formation of the front.

4.3.3. *Convergence Analysis.* To rigorously assess the numerical convergence of the proposed scheme, we quantify the error in the particle distribution using the Wasserstein-2 distance. Given the Lagrangian nature of the solution, the error at time t is defined between the approximate solution and a high-resolution reference solution

$$\text{Error}(t) = W_2 \left(\sum_{i=1}^N m^i \delta_{\mathbf{z}^i(t)}, \sum_{j=1}^{N_{\text{ref}}} m_{\text{ref}}^j \delta_{\mathbf{z}_{\text{ref}}^j(t)} \right). \quad (4.25)$$

Because the semi-geostrophic equations are known to be sensitive to (see [15]), we restrict our convergence analysis to day one. This ensures we are measuring the convergence of the numerical scheme rather than the divergence of the physical system.

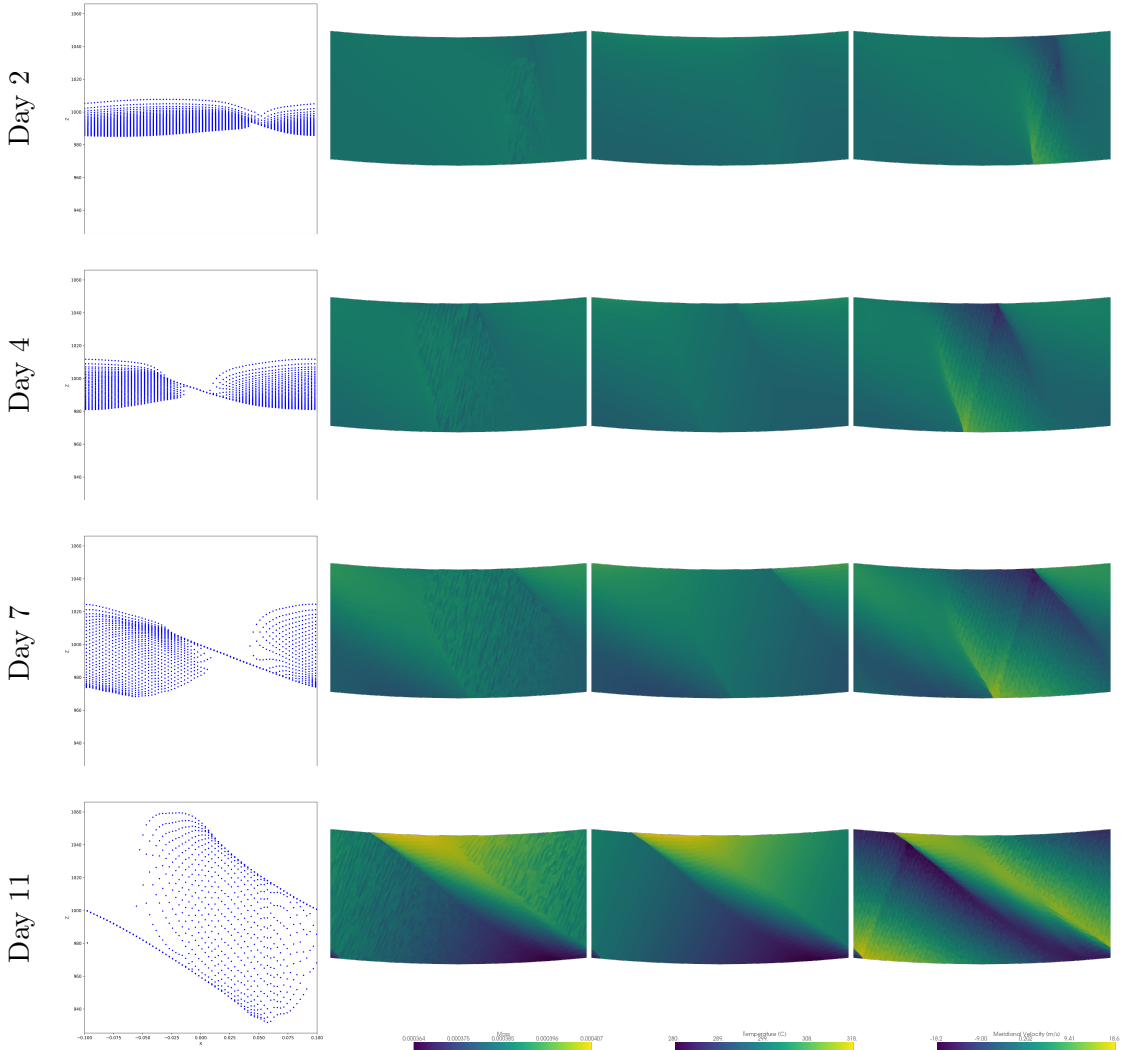


FIGURE 3. Evolution of particle positions (column 1), velocity (column 2), temperature (column 3), and mass (column 4) over days 2, 4, 7, and 11. Unlike the reference solution [18], the front exhibits horizontal drift and elongation due to the definition of Π_0 .

Figure 5 shows the convergence with respect to the timestep size h , comparing against a reference simulation with $h_{\text{ref}} = 15\text{min}$. Since the number of particles N is fixed for this study, the transport map between the solutions is the identity. We therefore compute the error using a normalized mass-weighted Euclidean norm:

$$\text{Error}(t) = \frac{1}{C} \sqrt{\sum_{i=1}^N m^i \|\mathbf{z}^i(t) - \mathbf{z}_{\text{ref}}^i(t)\|^2}. \quad (4.26)$$

Although we employ a second-order Adams-Bashforth (AB2) time-integration scheme, the results in Figure 5 exhibit a convergence rate closer to first-order. This reduction in order is attributed to the lack of global smoothness in the internal energy term, E_I . As shown in the single seed benchmark, E_I is only piecewise smooth; the presence of “kinks” in the energy landscape introduces discontinuities in the derivatives of the velocity field, which degrades the theoretical order of the ODE solver.

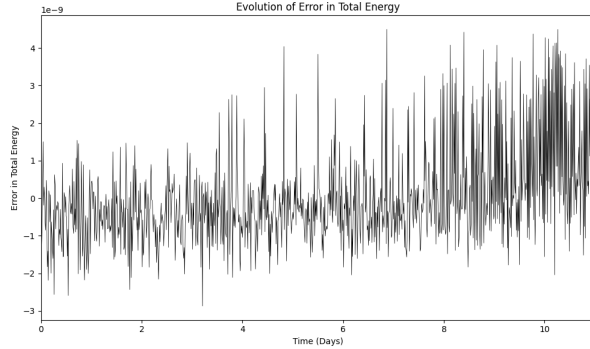


FIGURE 4. Evolution of the relative error in total geostrophic energy (Eq. 4.24). The error remains bounded, demonstrating the stability of the symplectic-like optimal transport integration.

Figure 6 presents the convergence with respect to the spatial resolution, i.e. the number of particles N . Here, we compare against a high-resolution reference with $N_{\text{ref}} = 2592$. Because the particle indices do not correspond between simulations of different sizes, we compute the W_2 distance by solving the optimal transport problem directly. To handle slight variations in total mass and discretization, we utilize the *OTT-JAX* library to solve the entropic Unbalanced Sinkhorn problem, taking the square root of the transport cost to return the distance metric.

The results show a convergence rate of approximately $\mathcal{O}(N^{-\frac{1}{2}})$. This result is consistent with the theoretical optimal quantization rate for measures in two dimensions. As established in [13], the optimal approximation of an absolutely continuous measure by a discrete set of N points scales as $W_p \sim N^{-\frac{1}{d}}$. For our 2D slice model ($d = 2$), this implies $W_2 \sim N^{-\frac{1}{2}}$, confirming that our scheme achieves the optimal spatial convergence rate allowed by the discretization.

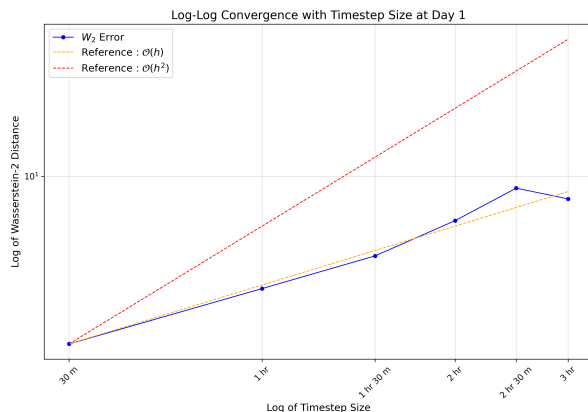


FIGURE 5. Timestep Error Convergence. Simulations investigating the impact of h were done with $N = 2592$. The scheme exhibits first-order convergence due to the non-smoothness of the internal energy field.

ACKNOWLEDGEMENTS

We thank Colin Cotter and Hiroe Yamazaki for stimulating discussions related to this work and sharing early drafts of their work. We thank Quentin M erigot and Hugo Leclerc for their support in implementing the code. We thank David Bourne for his invaluable advice and suggestions throughout the process. TPL was supported by The Maxwell Institute Graduate School in Modelling, Analysis, and Computation, a Centre for Doctoral Training funded by the EPSRC (grant EP/S023291/1), the Scottish Funding Council, Heriot-Watt University and the

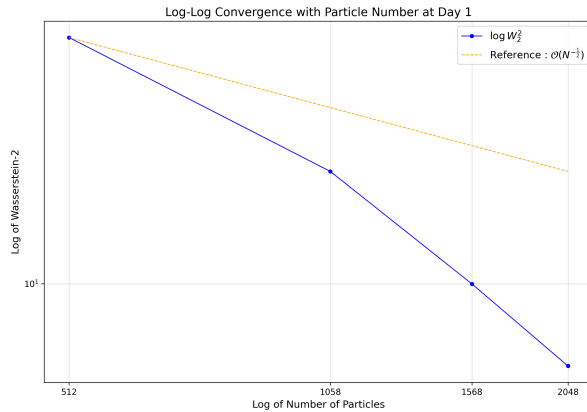


FIGURE 6. Particle Error Convergence. Simulations investigating the impact of N were done with $h = 5400$. The observed slope of $-\frac{1}{2}$ is consistent with the optimal quantization rate for 2D measures ($W_2 \propto N^{-\frac{1}{2}}$)

University of Edinburgh. BP gratefully acknowledges the support of the EPSRC via the grant EP/P011543/1.

REFERENCES

- [1] J.-D. Benamou and Y. Brenier. Weak existence for the semigeostrophic equations formulated as a coupled Monge-Ampère/transport problem. *SIAM Journal on Applied Mathematics*, 58(5):1450–1461, 1998.
- [2] J.-D. Benamou, C. Cotter, and H. Malamut. Entropic optimal transport solutions of the semigeostrophic equations. *Journal of Computational Physics*, 500:112745, 2024.
- [3] J.-D. Benamou, C. J. Cotter, J. J. M. Francis, and H. Malamut. Entropic approximations of the semigeostrophic shallow water equations, 2025.
- [4] D. Bourne, M. Pearce, and S. Roper. Geometric modelling of polycrystalline materials: Laguerre tessellations and periodic semi-discrete optimal transport. *Mechanics Research Communications*, 127:104023, 2023.
- [5] D. P. Bourne, C. P. Egan, T. Lavier, and B. Pelloni. Semi-discrete optimal transport techniques for the compressible semi-geostrophic equations. *SIMA*, *in press*, 2025.
- [6] G. Carlier and H. Malamut. Well-posedness and convergence of entropic approximation of semi-geostrophic equations, 2024.
- [7] C. J. Cotter and D. D. Holm. A variational formulation of vertical slice models. *Proceedings of the Royal Society A: Mathematical, Physical and Engineering Sciences*, 469(2155):20120678, 7 2013.
- [8] M. Cullen and H. Maroofi. The Fully Compressible Semi-Geostrophic System from Meteorology. *Archive for Rational Mechanics and Analysis*, 167(4):309–336, 5 2003.
- [9] C. P. Egan, D. P. Bourne, C. J. Cotter, M. J. P. Cullen, B. Pelloni, S. M. Roper, and M. Wilkinson. A new implementation of the geometric method for solving the Eady slice equations. *Journal of Computational Physics*, 469:111542, 2022.
- [10] T. O. Gallouët and Q. Mérigot. A Lagrangian scheme à la Brenier for the incompressible euler equations. *Foundations of Computational Mathematics*, 18(4):835–865, Aug 2018.
- [11] B. J. Hoskins. The geostrophic momentum approximation and the semi-geostrophic equations. *Journal of the Atmospheric Sciences*, 32(2):233–242, 1975.
- [12] J. Kitagawa, Q. Mérigot, and B. Thibert. Convergence of a Newton algorithm for semi-discrete optimal transport. *Journal of the European Mathematical Society*, 21(9):2603–2651, 2019.
- [13] B. Kloeckner. Approximation by finitely supported measures. *ESAIM: Control, Optimisation and Calculus of Variations*, 18(2):343–359, 7 2012.

- [14] T. Lavier. *Optimal Transport Techniques for Atmospheric Dynamics*. PhD thesis, Heriot-Watt University, 2025.
- [15] T. Lavier. A semi-discrete optimal transport scheme for the 3d incompressible semi-geostrophic equations. *IMA Journal of Applied Mathematics*, page hxaf023, 12 2025.
- [16] J. Meyron. Initialization Procedures for Discrete and Semi-Discrete Optimal Transport. *Computer-Aided Design*, 115:13–22, 10 2019.
- [17] Q. Mérigot and B. Thibert. Chapter 2 - optimal transport: discretization and algorithms. In A. Bonito and R. H. Nochetto, editors, *Geometric Partial Differential Equations - Part II*, volume 22 of *Handbook of Numerical Analysis*, pages 133–212. Elsevier, 2021.
- [18] H. Yamazaki and C. J. Cotter. A vertical slice frontogenesis test case for compressible nonhydrostatic dynamical cores of atmospheric models. *arXiv:2501.09752*, 2025.

APPENDIX A. INTEGRAL REDUCTIONS

In the following we will always parametrize a path between two vertices \mathbf{p}^j and \mathbf{p}^{j+1} with $\gamma : \mathbb{R} \rightarrow \mathbb{R}^d$ given by

$$\gamma(s) = s\mathbf{p}^{j+1} + (1-s)\mathbf{p}^j, \quad (\text{A.1})$$

where d is the dimension we are working in. In two dimensions we have the following cost function

$$c(\mathbf{x}, \mathbf{y}) = \frac{1}{y_2} \left(\frac{f_{\text{cor}}^2}{2} (x_1 - y_1)^2 + gx_2 \right) - c_p \Pi_0, \quad (\text{A.2})$$

and

$$\Phi(\mathbf{p}; \mathbf{y}) \text{ with } \mathbf{y} = \begin{bmatrix} 0 \\ 1 \end{bmatrix}, \quad (\text{A.3})$$

so that

$$\Phi(\mathbf{p}) = \begin{bmatrix} \frac{p_1}{f_{\text{cor}}^2} \\ \frac{1}{g} \left(p_2 - \frac{p_1^2}{2f_{\text{cor}}^2} \right) \end{bmatrix}, \quad (\text{A.4})$$

and

$$D\Phi = \begin{pmatrix} f_{\text{cor}}^{-2} & 0 \\ -f_{\text{cor}}^{-2} p_1 & g^{-1} \end{pmatrix} \text{ and } |\det D\Phi| = \frac{1}{f_{\text{cor}}^2 g}. \quad (\text{A.5})$$

In two dimensions \mathbf{n} is the normal vector to the edge between two cells and K^i is the number of vertices of the i th cell.

By letting

$$\mathbf{y}^i(\mathbf{z}^i) = \mathbf{y}^i = \frac{1}{2z_2^i} \begin{bmatrix} z_1^i \\ -1 \end{bmatrix}, \quad (\text{A.6})$$

$$\psi^i(\mathbf{z}^i, w^i) = w^i + \left(\frac{z_1^i}{2z_2^i} \right)^2 + \left(\frac{1}{2z_2^i} \right)^2 - \frac{f_{\text{cor}}^2}{2z_2^i} (z_1^i)^2 + c_p \Pi_0, \quad (\text{A.7})$$

then

$$\begin{aligned} c(\Phi(\mathbf{p}), \mathbf{z}^i) - w^i - c(\Phi(\mathbf{p}), \mathbf{z}^j) + w^j &= \|\mathbf{p} - \mathbf{y}^i\|^2 - \|\mathbf{p}\|^2 - \psi^i - \|\mathbf{p} - \mathbf{y}^j\|^2 + \|\mathbf{p}\|^2 + \psi^j \\ &= \|\mathbf{p} - \mathbf{y}^i\|^2 - \psi^i - \|\mathbf{p} - \mathbf{y}^j\|^2 + \psi^j. \end{aligned}$$

A.1. Gradient. In the two dimensional problem the gradient is given by

$$\frac{\partial \mathcal{G}}{\partial w^i} = m^i - \int_{L_c^i(\mathbf{w}, \mathbf{z})} (f^*)'(w^i - c(\mathbf{x}, \mathbf{z}^i)) d\mathcal{H}^2. \quad (\text{A.8})$$

We can reduce the integral to an evaluation at the vertices as by using the divergence theorem with

$$\mathbf{F} = \begin{bmatrix} 0 \\ -z_2^i f^*(w^i - c(\Phi(\mathbf{p}), \mathbf{z}^i)) \end{bmatrix}, \quad (\text{A.9})$$

as follows

$$\begin{aligned} & \int_{L_c^i(\mathbf{w}, \mathbf{z})} (f^*)'(w^i - c(\mathbf{x}, \mathbf{z}^i)) d\mathcal{H}^2 \\ &= \frac{1}{f_{\text{cor}}^2 g} \int_{\Phi^{-1}(L_c^i(\mathbf{w}, \mathbf{z}))} (f^*)'(w^i - c(\Phi(\mathbf{p}), \mathbf{z}^i)) d\mathcal{H}^2 \\ &= \frac{1}{f_{\text{cor}}^2 g} \int_{\partial \Phi^{-1}(L_c^i(\mathbf{w}, \mathbf{z}))} \mathbf{F} \cdot \mathbf{n} d\mathcal{H}^1 \\ &= - \sum_{j=1}^{K^i} \frac{z_2^i n_2}{f_{\text{cor}}^2 g} \|\mathbf{p}^{j+1} - \mathbf{p}^j\| \int_0^1 f^*(w^i - c(\Phi(\gamma(s)), \mathbf{z}^i)) ds. \end{aligned}$$

A.2. **Hessian.** In the two dimensional problem the Hessian is given by

$$\frac{\partial^2 \mathcal{G}}{\partial w^i \partial w^j}(\mathbf{w}, \mathbf{z}) = \int_{L_c^i(\mathbf{w}, \mathbf{z}) \cap L_c^j(\mathbf{w}, \mathbf{z})} \frac{1}{\|\nabla_{\mathbf{x}} u^{ij}(\mathbf{x})\|} (f^*)'(w^i - c(\mathbf{x}, \mathbf{z}^i)) d\mathcal{H}^1 \quad (\text{A.10})$$

$$\begin{aligned} \frac{\partial^2 \mathcal{G}}{\partial w^i \partial w^i}(\mathbf{w}, \mathbf{z}) &= - \int_{L_c^i(\mathbf{w}, \mathbf{z})} (f^*)''(w^i - c(\mathbf{x}, \mathbf{z}^i)) d\mathcal{H}^2 \\ &\quad - \sum_{i \neq j} \int_{L_c^i(\mathbf{w}, \mathbf{z}) \cap L_c^j(\mathbf{w}, \mathbf{z})} \frac{1}{\|\nabla_{\mathbf{x}} u^{ij}(\mathbf{x})\|} (f^*)'(w^i - c(\mathbf{x}, \mathbf{z}^i)) d\mathcal{H}^1. \end{aligned} \quad (\text{A.11})$$

We'll handle the two integrals separately. First we will handle the integral with the second derivative by using the divergence theorem with

$$\mathbf{F} = \begin{bmatrix} 0 \\ -z_2^i (f^*)'(w^i - c(\Phi(\mathbf{p}), \mathbf{z}^i)) \end{bmatrix}, \quad (\text{A.12})$$

as follows

$$\begin{aligned} &\int_{L_c^i(\mathbf{w}, \mathbf{z})} (f^*)''(w^i - c(\mathbf{x}, \mathbf{z}^i)) d\mathcal{H}^2 \\ &= \frac{1}{f_{\text{cor}}^2 g} \int_{\Phi^{-1}(L_c^i(\mathbf{w}, \mathbf{z}))} (f^*)''(w^i - c(\Phi(\mathbf{p}), \mathbf{z}^i)) d\mathcal{H}^2 \\ &= \frac{1}{f_{\text{cor}}^2 g} \int_{\partial \Phi^{-1}(L_c^i(\mathbf{w}, \mathbf{z}))} \mathbf{F} \cdot \mathbf{n} d\mathcal{H}^1 \\ &= \sum_{j=1}^{K^i} -\frac{z_2^i n_2}{f_{\text{cor}}^2 g} \|\mathbf{p}^{j+1} - \mathbf{p}^j\| \int_0^1 (f^*)'(w^i - c(\Phi(\gamma(s)), \mathbf{z}^i)) ds. \end{aligned}$$

Now we will handle the integral with the first derivative using the path parametrisation but first define

$$g(\mathbf{x}) = \|\nabla_{\mathbf{x}} u^{ik}(\mathbf{x})\| = \sqrt{g^2 \left(\frac{1}{z_2^i} - \frac{1}{z_2^k} \right)^2 + f_{\text{cor}}^4 \left(\frac{z_2^i z_1^k - z_1^i z_2^k + x_1 (z_2^k - z_2^i)}{z_2^i z_2^k} \right)^2}, \quad (\text{A.13})$$

letting

$$\begin{aligned} A_1 &= \frac{(p_1^{j+1} - p_1^j)^2 (z_2^i - z_2^k)^2}{(z_2^i)^2 (z_2^k)^2} \\ A_2 &= \frac{2(p_1^{j+1} - p_1^j)(z_2^i - z_2^k)(p_1^j(z_2^i - z_2^k) + f_{\text{cor}}^2(z_1^i z_2^k - z_2^i z_1^k))}{(z_2^i)^2 (z_2^k)^2} \\ A_3 &= \frac{g^2 (z_2^i - z_2^k)^2 + (p_1^j(z_2^i - z_2^k) + f_{\text{cor}}^2(z_1^i z_2^k - z_2^i z_1^k))^2}{(z_2^i)^2 (z_2^k)^2}, \end{aligned}$$

so that

$$g(\Phi(\gamma(s))) = \sqrt{A_1 s^2 + A_2 s + A_3}. \quad (\text{A.14})$$

and therefore,

$$\begin{aligned} &\int_{L_c^i(\mathbf{w}, \mathbf{z}) \cap L_c^k(\mathbf{w}, \mathbf{z})} \frac{1}{\|\nabla_{\mathbf{x}} u^{ik}(\mathbf{x})\|} (f^*)'(w^i - c(\mathbf{x}, \mathbf{z}^i)) d\mathcal{H}^1 \\ &= \int_0^1 \frac{(f^*)'(w^i - c(\Phi(\gamma(s)), \mathbf{z}^i))}{g(\Phi(\gamma(s)))} \|D\Phi(\gamma(s)) \cdot (\mathbf{p}^{j+1} - \mathbf{p}^j)\| ds. \end{aligned}$$

A.3. **Centroid.** In the two dimensional problem the centroid is given by

$$\mathbf{C}^i(\mathbf{z}) = \int_{L_c^i(\mathbf{w}, \mathbf{z})} \mathbf{x}(f^*)'(w^i - c(\mathbf{x}, \mathbf{z}^i)) d\mathcal{H}^2. \quad (\text{A.15})$$

We can reduce the integral to an evaluation at the vertices as by using the divergence theorem with

$$\mathbf{F}_1 = \begin{bmatrix} 0 \\ -z_2^i p_1 f^*(w^i - c(\Phi(\mathbf{p}), \mathbf{z}^i)) \end{bmatrix} \quad (\text{A.16})$$

$$\mathbf{F}_2 = \begin{bmatrix} \frac{p_2 z_2^i}{z_1^i} f^*(w^i - c(\Phi(\mathbf{p}), \mathbf{z}^i)) \\ 0 \end{bmatrix} \quad (\text{A.17})$$

$$\mathbf{F}_3 = \begin{bmatrix} 0 \\ -z_2^i p_1^2 f^*(w^i - c(\Phi(\mathbf{p}), \mathbf{z}^i)) \end{bmatrix}. \quad (\text{A.18})$$

We handle the components separately,

$$\begin{aligned} & \int_{L_c^i(\mathbf{w}, \mathbf{z})} x_1(f^*)'(w^i - c(\mathbf{x}, \mathbf{z}^i)) d\mathcal{H}^2 \\ &= \frac{1}{f_{\text{cor}}^2 g} \int_{\Phi^{-1}(L_c^i(\mathbf{w}, \mathbf{z}))} \frac{p_1}{f_{\text{cor}}^2} (f^*)'(w^i - c(\Phi(\mathbf{p}), \mathbf{z}^i)) d\mathcal{H}^2 \\ &= \frac{1}{f_{\text{cor}}^4 g} \int_{\partial\Phi^{-1}(L_c^i(\mathbf{w}, \mathbf{z}))} \mathbf{F}_1 \cdot \mathbf{n} d\mathcal{H}^1 \\ &= \sum_{j=1}^{K^i} -\frac{z_2^i n_2}{f_{\text{cor}}^4 g} \|\mathbf{p}^{j+1} - \mathbf{p}^j\| \int_0^1 \gamma_1(s) f^*(w^i - c(\Phi(\gamma(s)), \mathbf{z}^i)) ds. \end{aligned}$$

Now the other component,

$$\begin{aligned} & \int_{L_c^i(\mathbf{w}, \mathbf{z})} x_2(f^*)'(w^i - c(\mathbf{x}, \mathbf{z}^i)) d\mathcal{H}^2 \\ &= \frac{1}{f_{\text{cor}}^2 g} \int_{\Phi^{-1}(L_c^i(\mathbf{w}, \mathbf{z}))} \frac{1}{g} \left(p_2 - \frac{p_1^2}{2f_{\text{cor}}^2} \right) (f^*)'(w^i - c(\Phi(\mathbf{p}), \mathbf{z}^i)) d\mathcal{H}^2 \\ &= \frac{1}{f_{\text{cor}}^2 g^2} \int_{\partial\Phi^{-1}(L_c^i(\mathbf{w}, \mathbf{z}))} \mathbf{F}_2 \cdot \mathbf{n} d\mathcal{H}^1 - \frac{1}{2f_{\text{cor}}^4 g^2} \int_{\partial\Phi^{-1}(L_c^i(\mathbf{w}, \mathbf{z}))} \mathbf{F}_3 \cdot \mathbf{n} d\mathcal{H}^1 \\ &= \sum_{j=1}^{K^i} \frac{z_2^i n_1}{z_1^i f_{\text{cor}}^2 g^2} \|\mathbf{p}^{j+1} - \mathbf{p}^j\| \int_0^1 \gamma_2(s) f^*(w^i - c(\Phi(\gamma(s)), \mathbf{z}^i)) ds \\ &\quad + \frac{z_2^i n_2}{2f_{\text{cor}}^4 g^2} \|\mathbf{p}^{j+1} - \mathbf{p}^j\| \int_0^1 (\gamma_1(s))^2 f^*(w^i - c(\Phi(\gamma(s)), \mathbf{z}^i)) ds. \end{aligned}$$

A.4. **Internal Energy.** The final integral that we need to evaluate in two dimensions is the internal energy due to the compressibility and thermodynamics. This is given by

$$\Pi_0 \int_{L_c^i(\mathbf{w}, \mathbf{z})} (f^*)'(w^i - c(\mathbf{x}, \mathbf{z}^i)) d\mathcal{H}^2 - \left(\frac{R_d}{p_0} \right)^{\gamma-1} \int_{L_c^i(\mathbf{w}, \mathbf{z})} ((f^*)'(w^i - c(\mathbf{x}, \mathbf{z}^i)))^\gamma d\mathcal{H}^2. \quad (\text{A.19})$$

The second term is just a scaled version of the integral that we evaluated for the gradient so that one is already handled. We need to treat first term separately. By choosing

$$\mathbf{F} = \begin{bmatrix} 0 \\ -\frac{z_2^i(\gamma-1)}{(2\gamma-1)} (w^i - c(\Phi(\mathbf{p}), \mathbf{z}^i)) ((f^*)'(w^i - c(\Phi(\mathbf{p}), \mathbf{z}^i)))^\gamma \end{bmatrix}, \quad (\text{A.20})$$

we can apply the divergence theorem as follows

$$\int_{L_c^i(\mathbf{w}, \mathbf{z})} ((f^*)'(w^i - c(\mathbf{x}, \mathbf{z}^i)))^\gamma d\mathcal{H}^2$$

$$\begin{aligned}
&= \frac{1}{f_{\text{cor}g}^2} \int_{\Phi^{-1}(L_c^i(\mathbf{w}, \mathbf{z}))} ((f^*)'(w^i - c(\Phi(\mathbf{p}), \mathbf{z}^i)))^\gamma d\mathcal{H}^2 \\
&= \frac{1}{f_{\text{cor}g}^2} \int_{\partial\Phi^{-1}(L_c^i(\mathbf{w}, \mathbf{z}))} \mathbf{F} \cdot \mathbf{n} d\mathcal{H}^1 \\
&= -\frac{z_2^i n_2 (\gamma - 1)}{f_{\text{cor}g}^2 (2\gamma - 1)} \int_{\partial\Phi^{-1}(L_c^i(\mathbf{w}, \mathbf{z}))} (w^i - c(\Phi(\mathbf{p}), \mathbf{z}^i)) ((f^*)'(w^i - c(\Phi(\mathbf{p}), \mathbf{z}^i)))^\gamma d\mathcal{H}^1 \\
&= \sum_{j=1}^{K^i} -\frac{z_2^i n_2 (\gamma - 1)}{f_{\text{cor}g}^2 (2\gamma - 1)} \|\mathbf{p}^{j+1} - \mathbf{p}^j\| \int_0^1 (w^i - c(\Phi(\gamma(s)), \mathbf{z}^i)) ((f^*)'(w^i - c(\Phi(\gamma(s)), \mathbf{z}^i)))^\gamma ds.
\end{aligned}$$